



D2.1: Modelling heat and mass transfer of novel redox porous structures

Lead beneficiary: IME

Due date: 30/04/2025 (M18)

Actual submission date: 30/04/2025 (M18)

Grant Agreement number	GA 101122206
Project acronym	SUN-to-LIQUID II
Project title	SUNlight-to-LIQUID: Efficient solar thermochemical synthesis of liquid hydrocarbon fuels using tailored porous-structured materials and heat recuperation
Type of action	Research and Innovation (RIA)
Start date of the project	01/11/2023
Duration	48 months
Project coordinator (organisation)	Dr Andreas Sizmann (Bauhaus Luftfahrt)
Phone	+49-171-3373210
E-mail	contact@sun-to-liquid-2.eu
Website	sun-to-liquid-2.eu



**Funded by
the European Union**

Project funded by



Schweizerische Eidgenossenschaft
Confédération suisse
Confederazione Svizzera
Confederaziun svizra

Swiss Confederation

Federal Department of Economic Affairs,
Education and Research EAER
**State Secretariat for Education,
Research and Innovation SERI**

Funded by the European Union under GA 101122206. Views and opinions expressed are however those of the author(s) only and do not necessarily reflect those of the European Union. Neither the European Union nor the granting authority can be held responsible for them.

This work has received funding from the Swiss State Secretariat for Education, Research and Innovation (SERI).

Document information

Document Name	D2.1: Modelling heat and mass transfer of novel redox porous structures
Version	VF
Version Date	30/04/2025
Author	José González-Aguilar, Manuel Romero, Germilly Barreto (IME)
Dissemination level	Public

Approvals

	Full Name	Organisation	Date
Coordinator	Andreas Sizmann	Bauhaus Luftfahrt (BHL)	29/04/2025
WP Leader	José González	IMDEA Energía (IME)	28/04/2025
Task Leader	José González	IMDEA Energía (IME)	28/04/2025
Other (Quality)	Julie CHUPIN	LUP	30/04/2025

Documents history

Version	Date	Modification	Name (Organisation)
01	29/04/2025	Version for revision	A. Sizmann (BHL)
02	30/04/2025	Final version for review	J. Gonzalez et al. (IME)
03	30/04/2025	Final version for submission	J. Gonzalez et al. (IME)
VF	30/04/2025	Quality check	J. CHUPIN (LUP)

Distribution list

Name	Organisation
SUN-to-LIQUID II Consortium	N/A
Project Officer Luca Bondi	EC / CINEA

Executive summary

This report presents a time dependent numerical modelling of heat and mass transfer in novel redox porous structures, a necessary tool to guide the selection of optimum material absorber structures and to support the design and further upscaling for the integration in solar reactors. A pore level ray tracing model, based on geometrical optics approach is coupled with Computational Fluid Dynamics (CFD) in COMSOL Multiphysics 6.2 to simulate and optimize porous geometries based on graded square-channelled configurations.

The focus is on the reduction step under vacuum conditions, where concentrated solar radiation propagation and absorption is solved by ray tracing approach. The infrared radiation transfer and heat conduction in the solid are solved using CFD, while the mass transfer related to the reduction of the material is computed using the resulting temperature field and temperature dependent stoichiometric correlations. The reduction material analysed is cerium oxide (CeO_2), with material properties and reference dimensions derived from well established results in literature. The simulated structure is a brick configuration composed of four layers, with a total height of 37.5 mm and a cross section of 25 mm x 25 mm. The walls have a constant thickness of 0.5 mm. The bottom layer (outlet) consists of 16x16 channels (finer channels), and the top layer, which receives in the first place the concentrated solar radiation, comprises 2x2 channels (larger channels). The intermediate layers have 8x8 (second layer) and 4x4 (third layer) channels.

The methodology involves coupling the ray tracing and the heat transfer models to simulate variations in layer heights under different incidence angles and solar fluxes, reflecting the spatial variation within a typical solar reactor cavity. A total of 760 simulations were conducted and the structures were evaluated using four figures of merit: (i) expected moles of oxygen released per kilogram of CeO_2 ; (ii) total moles of oxygen released; (iii) mass fraction of CeO_2 above 1000 °C; and (iv) mass fraction of CeO_2 above 1600 °C.

Results indicate that for low incidence angles of beam radiation (around 5° versus channel axis), the optimal configuration consists of two layers, half 16x16 channels and half 8x8 channels. As the beam incidence angle increases up to 20° – 30°, the third layer of 4x4 channels becomes beneficial, while the proportion of 16x16 channels should be reduced to about one quarter of the total height. In these conditions, the optimal configuration is made of three layers (16x16, 8x8 and 4x4 channels). At higher angles (30° and above), the 2x2 channels configuration starts to become beneficial, because it allows the concentrated solar radiation to propagate deeply in the structure, and the 4x4 becomes no more beneficial. In these conditions, the structure is made of 2 – 3 layers, excluding the 4x4 channels. In general, for low incidence angles, the best performing geometries have finer (8x8) channels at the top, while for higher angles larger channels are favourable at the top, but finer channels remain favourable at the bottom. Regarding different incident solar irradiance intensities, the top ranked structure based on moles of O_2 released per kilogram of CeO_2 remains almost unchanged, however slight changes are observed in the second to fourth rankings. Larger variations occur when ranking based on total moles of oxygen released is considered.

PROPRIETARY RIGHTS STATEMENT:

This document contains information which is proprietary to the SUN-to-LIQUID II consortium. Neither this document nor the information contained herein shall be used, duplicated or communicated by any means to any third party, in whole or in parts, except with the prior written consent of the SUN-to-LIQUID II consortium. This restriction legend shall not be altered nor obliterated on or from this document.

Table of contents

Executive summary	3
1. Introduction	8
2. Methodology	10
2.1. Introduction	10
2.2. General procedure – Structure of the basic block	10
2.3. Figures of merit	11
2.4. Numerical models – Boundary conditions - Mesh	11
3. Results	15
3.1. General trends – Figures of merit	15
3.2. General trends – Incident angle of radiation	18
3.3. General trends – Irradiance	20
3.4. Basic blocks ranking.....	20
4. Conclusions and Outlook	26
5. References	27

List of figures

Figure 1: Optimized square-grid structure and temperature distribution obtained in the work by Sas Brunser and Steinfeld (2023).	8
Figure 2: Geometry of basic block.	10
Figure 3: Mesh configuration with 1 mm cell elements.....	13
Figure 4: Different incidence angles (5°, 15°, 30° and 45°).	14
Figure 5: Solid fraction of the basic blocks versus the achieved mass for a temperature higher than 1000 °C and 1600 °C for the 35 possible arrangements. 5° of incidence angle and 1500 kW m ⁻² of incident flux.....	16
Figure 6: Solid fraction of the basic blocks versus the mass fraction for a temperature higher than 1000 °C and 1600 °C, for the 35 structural configurations, 5° of incidence angle and 1500 kW m ⁻² of incident flux.....	16
Figure 7: Solid fraction of the basic blocks versus the achieved mass for a temperature higher than 1000 °C and 1600 °C for the 35 possible arrangements. 30° of incidence angle and 1500 kW m ⁻² of incident flux.	17
Figure 8: Solid fraction of the basic blocks versus the mass fraction for a temperature higher than 1000 °C and 1600 °C, for the 35 structural configurations, 30° of incidence angle and 1500 kW m ⁻² of incident flux.....	17
Figure 9: Ranking of the 35 arrangements for 5° incidence angle and flux of 1500 kW m ⁻² in terms of number of mols released of O ₂ per unit of mass of the ceria basic block.	18

Figure 10: Ranking of the 35 arrangements for 15° incidence angle and flux of 1500 kW m⁻² in terms of number of mols released of O₂ per unit of mass of the ceria basic block.18

Figure 11: Ranking of the 35 arrangements for 30° incidence angle and flux of 1500 kW m⁻² in terms of number of mols released of O₂ per unit of mass of the ceria basic block.18

Figure 12: Ranking of the 35 arrangements for 45° incidence angle and flux of 1500 kW m⁻² in terms of number of mols released of O₂ per unit of mass of the ceria basic block.19

Figure 13: Ranking of the 35 arrangements for 5° incidence angle and flux of 1500 kW m⁻² in terms of number of mols released of O₂.19

Figure 14: Ranking of the 35 arrangements for 15° incidence angle and flux of 1500 kW m⁻² in terms of number of mols released of O₂.19

Figure 15: Ranking of the 35 arrangements for 30° incidence angle and flux of 1500 kW m⁻² in terms of number of mols released of O₂.20

Figure 16: Ranking of the 35 arrangements for 45° incidence angle and flux of 1500 kW m⁻² in terms of number of mols released of O₂.20

List of tables

Table 1: Best arrangements in terms of released oxygen per unit mass of ceria for different incidence angles and an incident flux of 1500 kW m⁻².22

Table 2: Best arrangements in terms of released oxygen for different incidence angles and an incident flux of 1500 kW m⁻².22

Table 3: Best arrangements in terms of fraction mass of zone at temperature higher than 1600 °C for different incidence angles and an incident flux of 1500 kW m⁻².23

Table 4: Best arrangements in terms of fraction mass of zone at temperature higher than 1000 °C for different incidence angles and an incident flux of 1500 kW m⁻².23

Table 5: Best arrangements in terms of released oxygen per unit mass of ceria for different incidence angles and an incident flux of 1000 kW m⁻².24

Table 6: Best arrangements in terms of released oxygen per unit mass of ceria for different incidence angles and an incident flux of 500 kW m⁻².24

Table 7: Best arrangements in terms of released oxygen for different incidence angles and an incident flux of 1000 kW m⁻².25

Table 8: Best arrangements in terms of released oxygen for different incidence angles and an incident flux of 500 kW m⁻².25

Glossary

Acronym	Signification
MC	Monte Carlo
RPC	Reticulated porous ceramic

1. Introduction

In the SUN-to-LIQUID II project, different stages are being addressed to increase the overall efficiency of solar-driven conversion of water and CO₂ to liquid fuels. One important step towards this goal is the optimization of the reactor structure for better absorption of concentrated solar radiation. In the recent work of Zoller et al. (2022), reticulated porous ceramics (RPC) were used in the previous EU Horizon2020 project SUN-to-LIQUID. Their results highlight the need on the optimization of the structure of the reactor, where they suggest that one of the directions is to replace the RPCs with 3D printed structured geometries to enhance solar radiation absorption and improve temperature homogeneity. These structures involve architectural improvements through 3D printing of redox materials with optical thickness gradually increasing from the illuminated surface toward the rear of the structure. This graded porosity, hierarchically ordered design, enables truly volumetric absorption, which homogenize the temperature across the structure and brings a much larger fraction of the material into the high-temperature window needed for higher solar-to-fuel energy conversion efficiencies.

Such structures, with a gradual increase in optical absorption toward the rear, have been analysed in previous studies available in literature. The most relevant is the work of Sas Brunser and Steinfeld (2023), which introduces a novel voxel-based Monte Carlo (MC) ray-tracing algorithm to simulate radiative heat transfer at the pore level in complex porous structures used in solar thermochemical reactors. Unlike the traditional RPC structures, which suffer from exponential radiation attenuation and inefficient fuel conversion, the study focused on hierarchically ordered porous structures that enhance volumetric radiation absorption and homogenize temperature distribution. They validated the algorithm through benchmark tests and experimental comparison, demonstrating its accuracy and substantial speed advantage. They then applied it in a gradient-free optimization framework to design three porous topologies: (i) square grids; (ii) Voronoi cells; (iii) and sphere lattices-optimized; for maximum solar fuel production based on a ceria based redox cycle. Among them, the optimized square-grid structure significantly outperformed the conventional RPC structure, achieving over four times the fuel yield per unit volume. The work not only demonstrated the effectiveness of voxel-based MC modelling for design and optimization, but also offers a pathway to improve the efficiency of solar-to-fuel energy conversion systems. Figure 1 shows the optimized square-grid structure and temperature distribution obtained in the work by Sas Brunser and Steinfeld (2023).

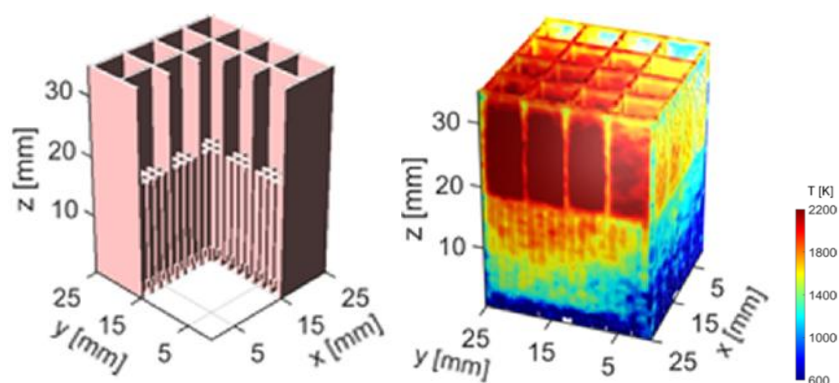


Figure 1: Optimized square-grid structure and temperature distribution obtained in the work by Sas Brunser and Steinfeld (2023).

In our work, we build upon such an optimized square-grid structure and provide beyond state-of-the-art designs, by more detailed modelling and optimization approaches under realistic operating conditions for CeO_2 based structures in solar reactors.

2. Methodology

2.1. Introduction

In a cavity reactor, concentrated solar rays reach the novel redox porous structure, based on CeO_2 , at different angles and intensities. To address this, a detailed time dependent model of a brick structure made of square-grid channels was developed for different structures configurations under different incidence angle and irradiance levels. The resulting structures are then ranked to identify the optimal configurations as a function of incidence angles and concentrated solar flux. This approach supports the design of optimized reactors aimed to achieve higher solar-to-fuel energy conversion efficiencies.

2.2. General procedure – Structure of the basic block

The geometry of the structure of the basic block analyzed in this work is illustrated in Figure 2. It has been assumed that the basic block is a stack of square channel monoliths and a maximum of four types of monoliths are sufficient to optimised the block performance. These four monoliths were composed of 16×16 square channels (finer channels), 8×8 , 4×4 , 2×2 channels (larger channels) arranged in an increasing channel size from the bottom to the top of the block. The total height of the block was fixed at 37.5 mm with a square cross-section of 25 mm x 25 mm, based on Sas Brunser and Steinfeld (2023). The height of each layer, $H_i, i = 1, \dots, 4$, is defined as a fraction f_i of the overall height H ,

$$H_i = f_i H, \quad i = 1, \dots, 4, \quad (1)$$

with

$$f_1 + f_2 + f_3 + f_4 = 1. \quad (2)$$

Besides, a constant wall thickness of 0.50 mm was assumed, which allows the channel widths for each layer to be automatically calculated based on the number of channels and the total cross-section size. Thus, the corresponding channel widths are: 1.03 mm for the first layer (16×16 channels), 2.56 mm for the second layer (8×8), 5.63 mm for the third layer (4×4 channels), and 11.75 mm for the fourth layer (2×2).

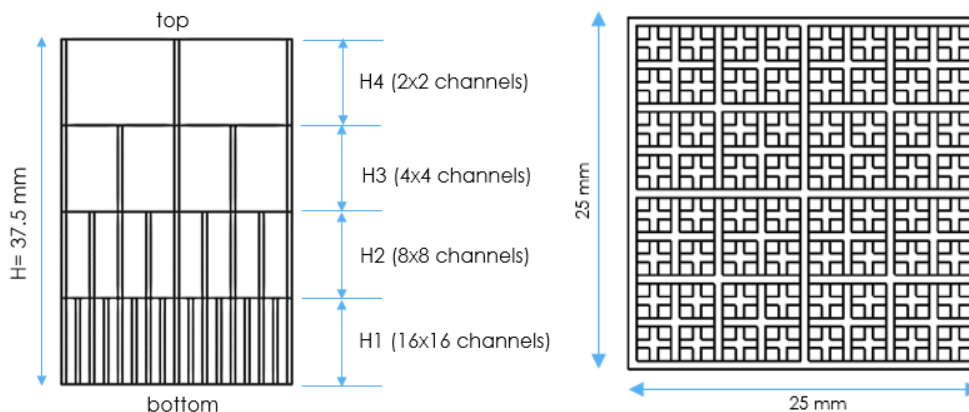


Figure 2: Geometry of basic block.

The optimisation of the structure was carried out considering all possible combinations of f_i ($i = 1, \dots, 4$) with values of 0.00, 0.25, 0.50, 0.75, and 1.00. This results in 35 possible configurations. Each combination is identified with the array (f_1, f_2, f_3, f_4) .

2.3. Figures of merit

Four figures of merit have been defined to quantify the performance of the basic blocks:

- Mass fraction of the solid volume which temperature is higher than 1000 °C, $\phi_{1000^\circ\text{C}}$;
- Mass fraction of the solid volume which temperature is higher than 1600 °C, $\phi_{1600^\circ\text{C}}$;
- Expected amount of released oxygen (in mol) according to the temperature distribution in the basic block, N_{O_2} ; and
- Expected amount of released oxygen per unit mass of CeO_2 , n_{O_2} .

The mass fraction of solid volume which temperature is above a given threshold, T_{th} , is calculated by

$$\phi_{T_{th}} = \frac{1}{M} \int_{T > T_{th}} \rho_{\text{CeO}_2} dV \quad (3)$$

where M is the total mass of the basic block and ρ_{CeO_2} is the effective bulk ceria density.

The redox material CeO_2 undergoes though an endothermic thermochemical reduction step described by the following reaction:



The amount of oxygen released is calculated by the formulation proposed by Bulfin et al. (2013),

$$\frac{\delta}{0.35 - \delta} = 8700 P_{\text{O}_2}^{-0.217} \exp\left(-\frac{195.6 \text{ kJ mol}^{-1}}{RT}\right) \quad (5)$$

Where δ is the oxygen non-stoichiometry, P_{O_2} is the partial pressure of oxygen (in Pa), R is the ideal gas constant ($8.3145 \text{ J mol}^{-1} \text{ K}^{-1}$), and T is the temperature (in K). A partial pressure of O_2 of 0.1 mbar is assumed for the calculations.

2.4. Numerical models – Boundary conditions - Mesh

For the numerical model, the reduction step is considered, which is the stage in which the system is illuminated with concentrated solar radiation. The solid redox material is assumed to be opaque, and the enthalpy change in the reduction process is neglected. Under these conditions, and assuming near vacuum environment, the relevant physical phenomena to model include radiation heat transfer (both visible and infrared) and heat conduction within the solid.

Radiation heat transfer is modelled using a ray tracing method. The propagation and absorption of the solar radiation are simulated using the “geometric optic” approach, which provides the spatial distribution of the absorbed solar radiation in the exposed surface of the solid material. Ray trajectories are computed using the Ray Optics

Module from COMSOL Multiphysics 6.2 (<https://www.comsol.com/>), which solves six coupled first-order ordinary differential equations for the components of the wave vector \mathbf{k} and the ray position vector in three-dimension space \mathbf{q} ,

$$\frac{d\mathbf{q}}{dt} = \frac{\partial \omega}{\partial \mathbf{k}} \quad (6)$$

$$\frac{d\mathbf{k}}{dt} = -\frac{\partial \omega}{\partial \mathbf{q}} \quad (7)$$

where \mathbf{k} represents the magnitude and direction of wave propagation, ω is the angular frequency, and t is time.

For thermal (infrared) radiation transfer, a radiative energy balance is solved using the radiosity method. The total radiosity or outgoing radiative flux from a given surface element (W m^{-2}), J , is:

$$J = -\varepsilon e_b(T) + \rho_d G \quad (8)$$

where ε is the surface emissivity, $e_b(T)$ is the blackbody emission at the local surface temperature T , ρ_d is the diffuse reflectivity, and G is the total radiative flux incident on the surface.

The time dependent heat transfer in the solid uniquely considers conduction and thus the energy conservation equation is:

$$\rho_{\text{CeO}_2} c_p \frac{\partial T}{\partial t} = \nabla \cdot (k \nabla T) \quad (9)$$

in which c_p is the heat capacity, k is the thermal conductivity. Both heat capacity and thermal conductivity are defined as temperature-dependent properties, which empirical formulations are (Furler et al., 2015) as follows:

$$c_p = \begin{cases} -0.0001271T^2 + 0.2697656T + 299.8695684 & \text{if } 280 < T \leq 1100 \text{ K} \\ 444.27 & \text{if } T > 1100 \text{ K} \end{cases} \quad (10)$$

$$k = \begin{cases} \frac{17.8004 - 0.02402T + 0.0000112032T^2 - 1.7 \cdot 10^{-9}T^3}{7.9799 + 0.00483384T - 9.3397 \cdot 10^{-6}T^2 + 2.8 \cdot 10^{-9}T^3} & \text{if } 280 < T \leq 2000 \text{ K} \\ 0.4 & \text{if } T > 2000 \text{ K} \end{cases} \quad (11)$$

The density of CeO_2 is taken as 7220 kg m^{-3} (Furler et al., 2015).

To solve the differential equations, each physics, i.e., ray tracing, infrared radiation transfer and heat condition in the solid, require boundary conditions. In the ray tracing and infrared radiation models, the top and internal walls are defined as diffuse scattering surfaces. For the ray tracing, these surfaces have an absorptivity of 0.7, as suggested by Sas Brunser and Seinfeld (2023). For the infrared radiation transfer, the

same surfaces are modelled as diffuse emittance with an emissivity of 0.7. the absorbed radiation at these boundaries is recorded and later applied as a boundary heat source in the heat transfer model. The external lateral and bottom walls are considered as non-active boundaries in the ray tracing model, meaning they do not participate in radiation exchange. The structure is opaque, with no radiation transmission through the material.

In the heat transfer model, the external lateral and bottom walls are considered adiabatic. The top and internal walls include a boundary heat source derived from the ray tracing results. The initial temperature of the entire domain is set to 25 °C.

The simulations are performed using COMSOL Multiphysics v6.2. Time dependent analysis is conducted for a total simulation time of 600 seconds, which corresponds to the duration of the reduction step reported by Zoller et al. (2022). Simulation results are saved at 60 seconds intervals.

A mesh sensitivity analysis was carried out, and it was found that a cell size of 1 mm provides sufficient accuracy and numerical stability for the model. [Figure 3](#) shows the mesh configuration with 1 mm cell elements. Additionally, for the ray tracing simulation, a total of 10^6 rays was used, offering a suitable balance between solution quality and computational cost.

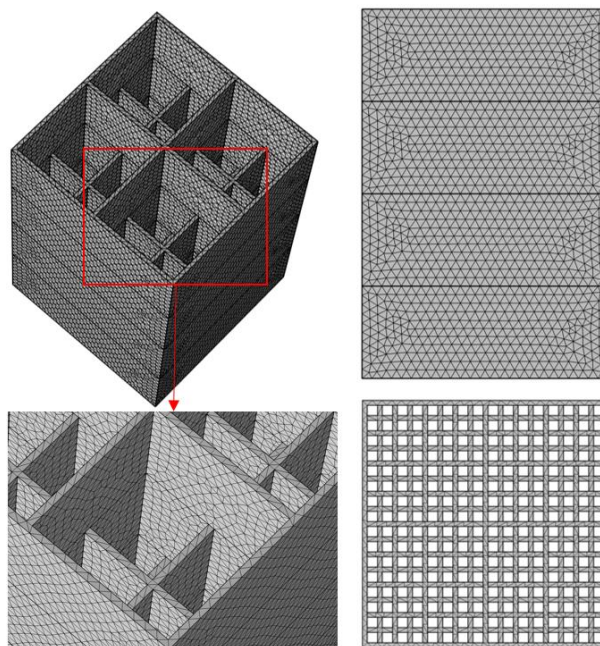


[Figure 3](#): Mesh configuration with 1 mm cell elements.

As discussed at the beginning of the document, to analyse the performance under conditions that emulate different regions of the reactor, four beam incidence angles are considered: 5°, 15°, 30° and 45°, as shown in [Figure 4](#). It is assumed that all rays launched from the light source release plane, defined as a projection of the brick inlet cross section area, are parallel (collimated).

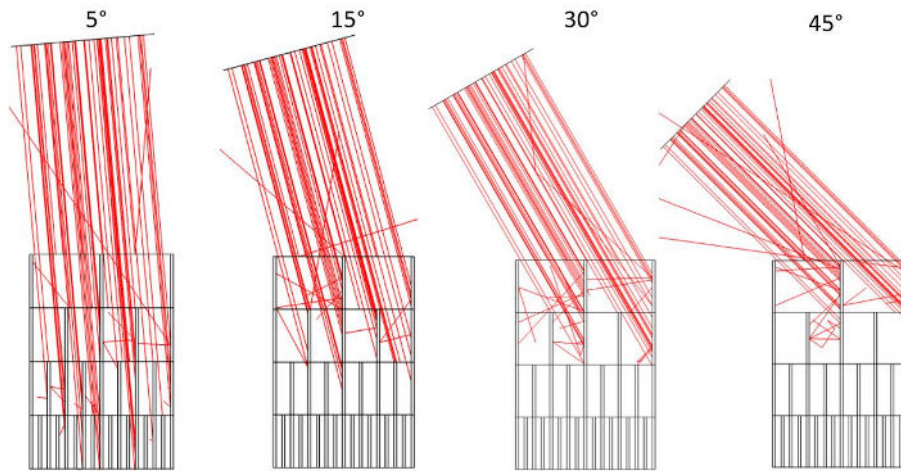


Figure 4: Different incidence angles (5°, 15°, 30° and 45°).

Regarding different incidence irradiances values, three different intensities were analysed: 1500 kW m^{-2} , 1000 kW m^{-2} , and 500 kW m^{-2} . In total, 760 simulations were performed to analyse trends and rank the structures according to all defined figures of merit described in Section 2.3.

3. Results

3.1. General trends – Figures of merit

An assessment of the performance established by the different figures of merit is carried out. [Figure 5](#) and [Figure 6](#) show the solid fraction of the basic blocks versus the achieved mass at a temperature higher than threshold values of 1000 °C and 1600 °C for the 35 possible arrangements of square channel monoliths when an incident beam impinges the block top surface with an incidence angle of 5° and irradiance of 1500 kW m⁻². [Figure 7](#) and [Figure 8](#) present the same results for an incidence angle of 30°, under the same irradiance conditions. As it can be seen, for an incident angle of 5°, the structure that achieves the highest performance both in terms of highest mass and mass fraction higher than the two threshold temperatures (1000 °C and 1600 °C) is $(f_1, f_2, f_3, f_4) = (1, 0, 0, 0)$. However, for higher incidence angles of 30°, the results reveal that the geometries with higher performance are $(f_1, f_2, f_3, f_4) = (0.5, 0.5, 0, 0)$ for 1000 °C and $(f_1, f_2, f_3, f_4) = (0.25, 0.75, 0, 0)$ for 1600 °C. However, these structures do not correspond to those with the larger mass fraction in temperature distribution. That is, they do not take advantage of a fraction of the ceria for releasing oxygen. The indicators n_{O_2} (mol O₂/kg CeO₂) and N_{O_2} (total moles of O₂ released) should be considered as the most relevant indicators, as they are the ones that reflect the amount of H₂ expected to be produced.

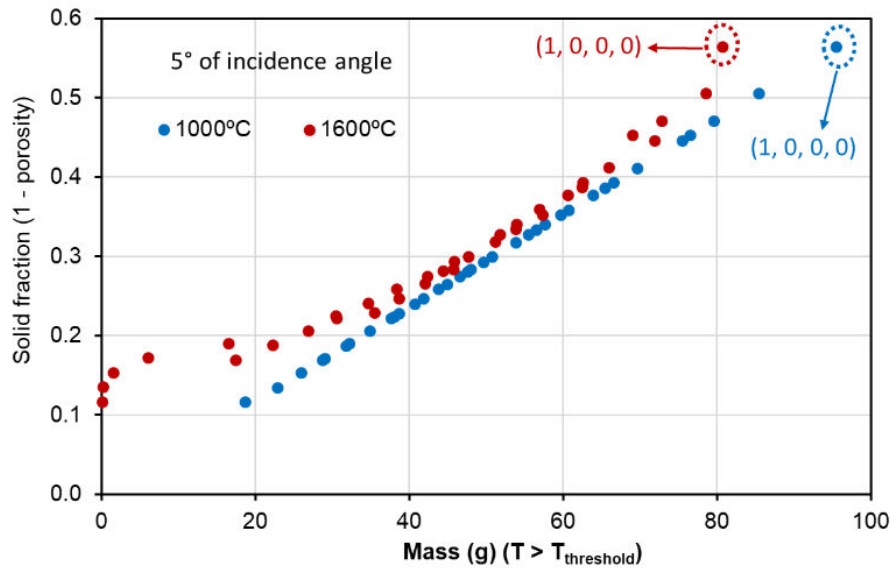


Figure 5: Solid fraction of the basic blocks versus the achieved mass for a temperature higher than 1000 °C and 1600 °C for the 35 possible arrangements. 5° of incidence angle and 1500 kW m⁻² of incident flux.

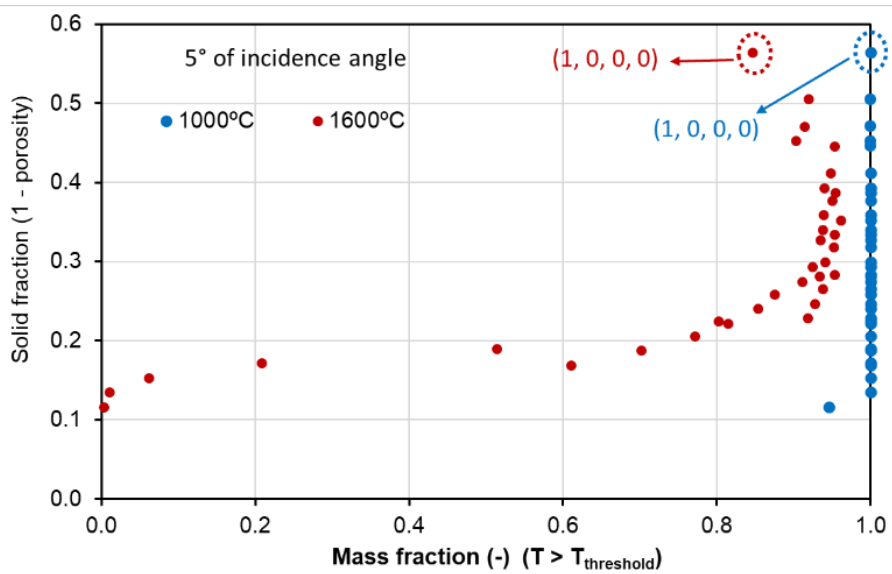


Figure 6: Solid fraction of the basic blocks versus the mass fraction for a temperature higher than 1000 °C and 1600 °C, for the 35 structural configurations, 5° of incidence angle and 1500 kW m⁻² of incident flux.

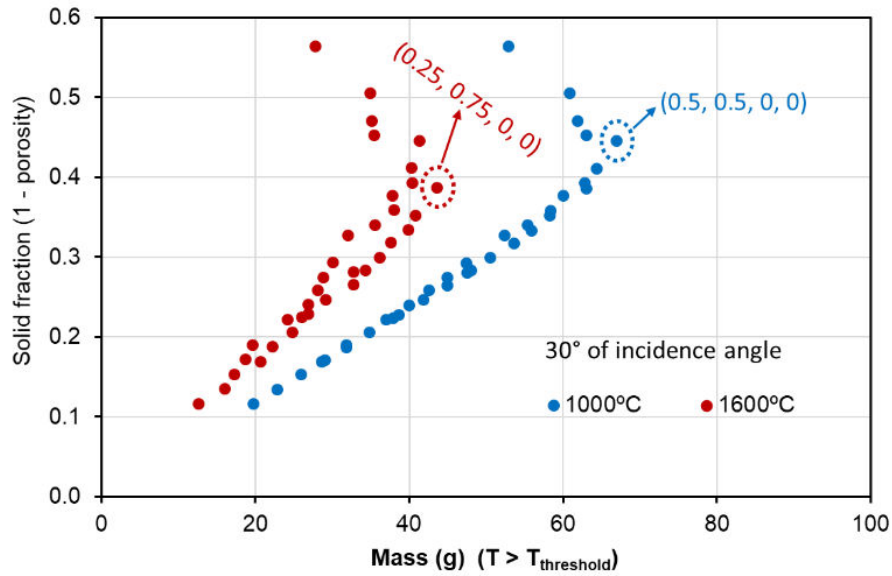


Figure 7: Solid fraction of the basic blocks versus the achieved mass for a temperature higher than 1000 °C and 1600 °C for the 35 possible arrangements. 30° of incidence angle and 1500 kW m⁻² of incident flux.

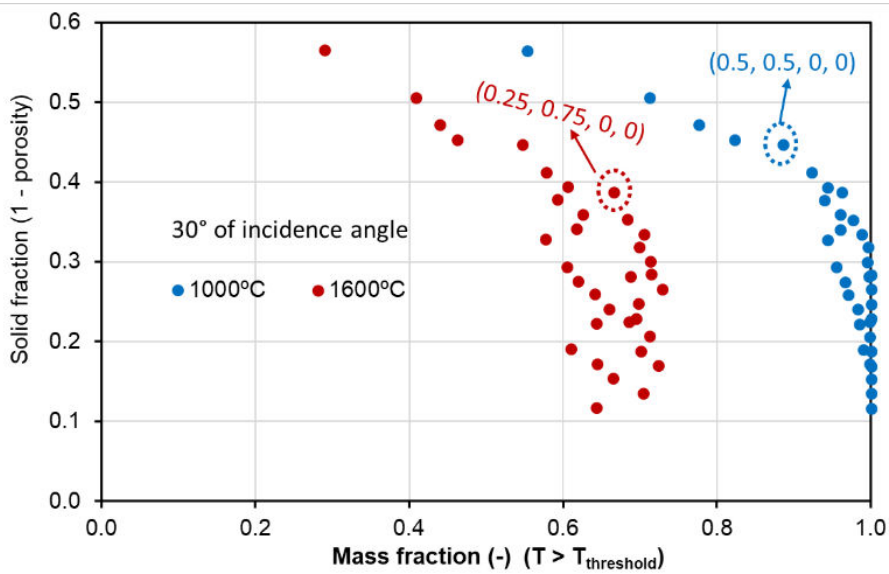


Figure 8: Solid fraction of the basic blocks versus the mass fraction for a temperature higher than 1000 °C and 1600 °C, for the 35 structural configurations, 30° of incidence angle and 1500 kW m⁻² of incident flux.

3.2. General trends – Incident angle of radiation

Figure 9, Figure 10, Figure 11, and Figure 12 show the 35 geometries ranked according to n_{O_2} for the four incidence angles: 5°, 15°, 30° and 45°, under a fixed incidence flux of 1500 kW m⁻². Similarly, Figure 13, Figure 14, Figure 15, and Figure 16 present the same geometries ordered based on N_{O_2} under same conditions.

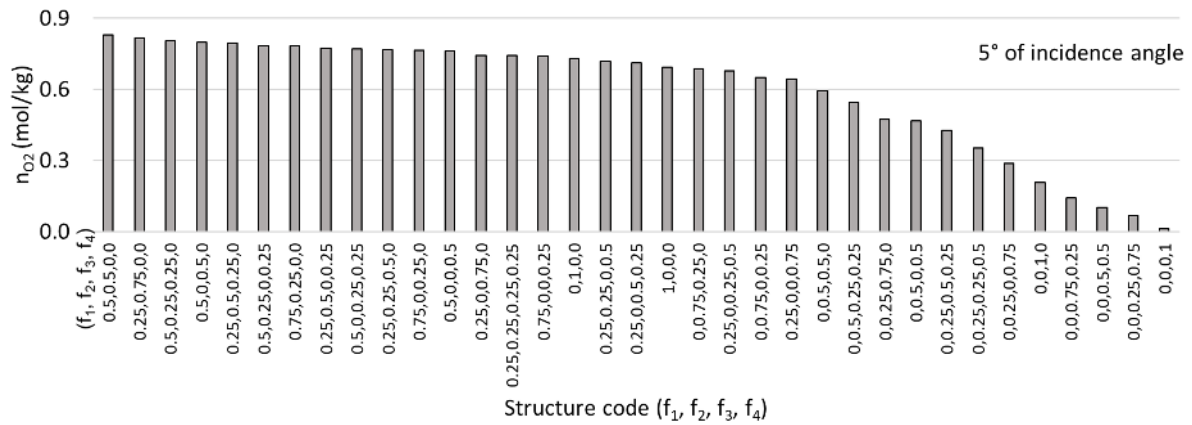


Figure 9: Ranking of the 35 arrangements for 5° incidence angle and flux of 1500 kW m⁻² in terms of number of mols released of O₂ per unit of mass of the ceria basic block.

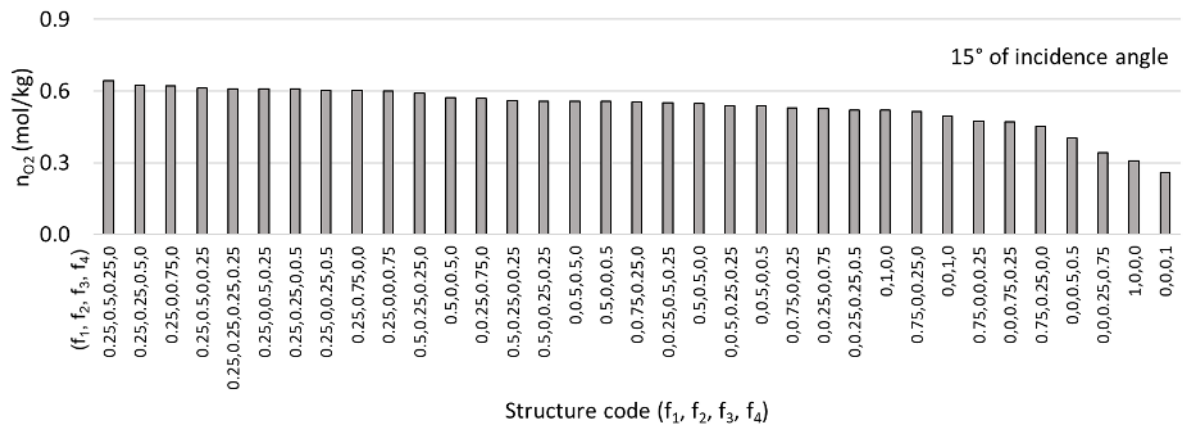


Figure 10: Ranking of the 35 arrangements for 15° incidence angle and flux of 1500 kW m⁻² in terms of number of mols released of O₂ per unit of mass of the ceria basic block.

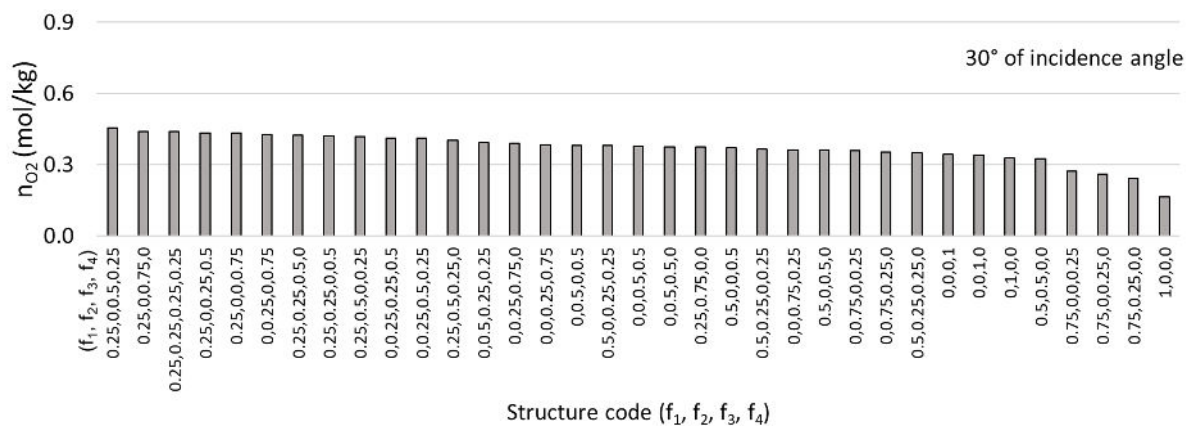


Figure 11: Ranking of the 35 arrangements for 30° incidence angle and flux of 1500 kW m⁻² in terms of number of mols released of O₂ per unit of mass of the ceria basic block.

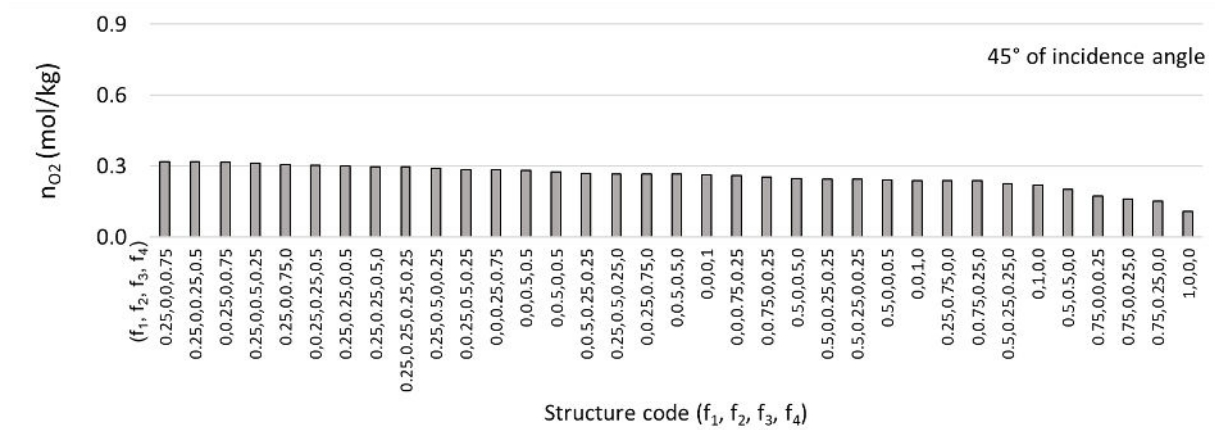


Figure 12: Ranking of the 35 arrangements for 45° incidence angle and flux of 1500 kW m⁻² in terms of number of mols released of O₂ per unit of mass of the ceria basic block.

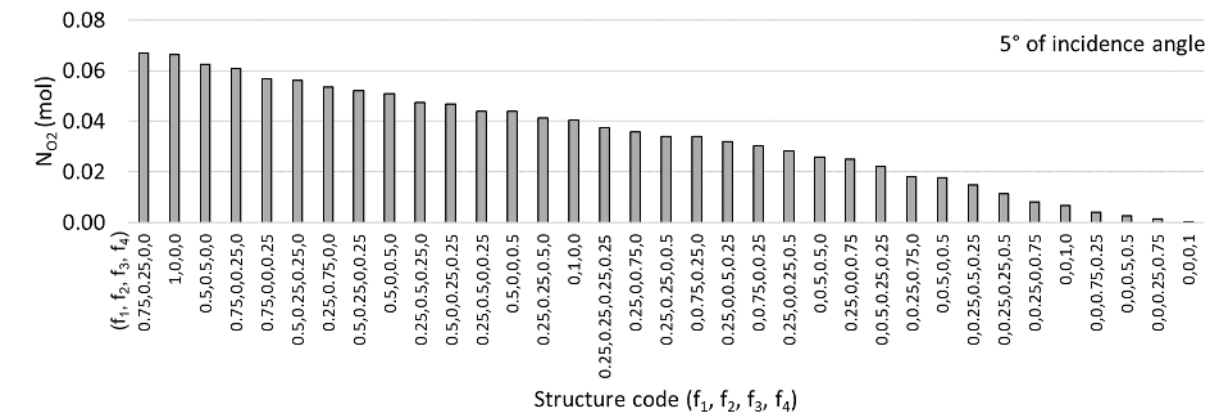


Figure 13: Ranking of the 35 arrangements for 5° incidence angle and flux of 1500 kW m⁻² in terms of number of mols released of O₂.

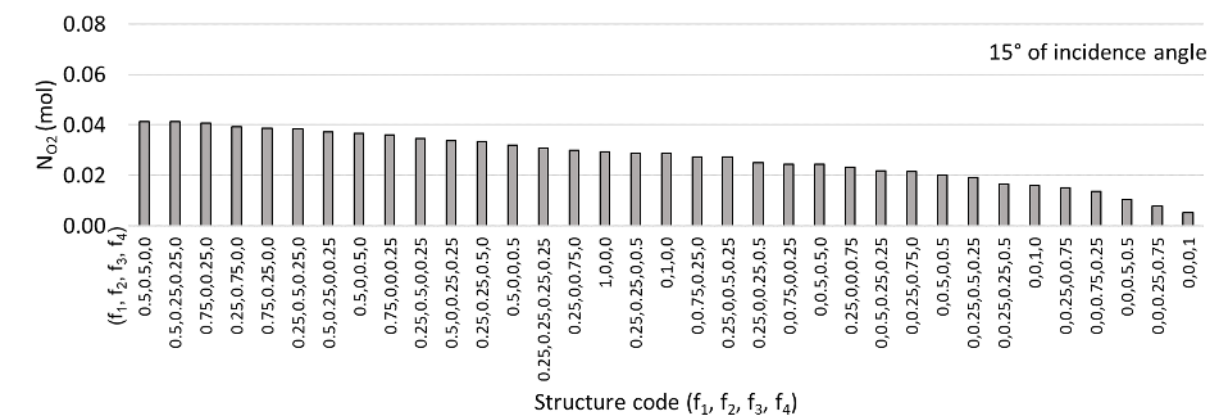


Figure 14: Ranking of the 35 arrangements for 15° incidence angle and flux of 1500 kW m⁻² in terms of number of mols released of O₂.

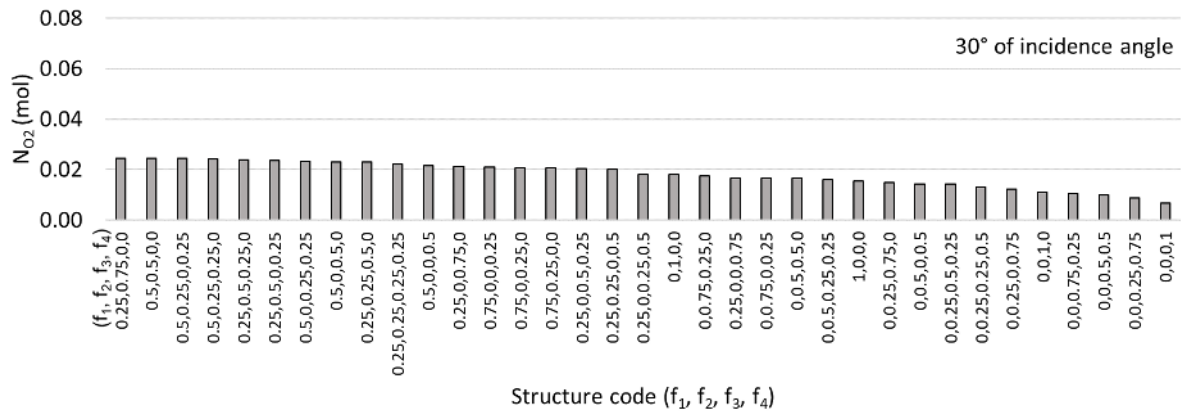


Figure 15: Ranking of the 35 arrangements for 30° incidence angle and flux of 1500 kW m⁻² in terms of number of mols released of O₂.

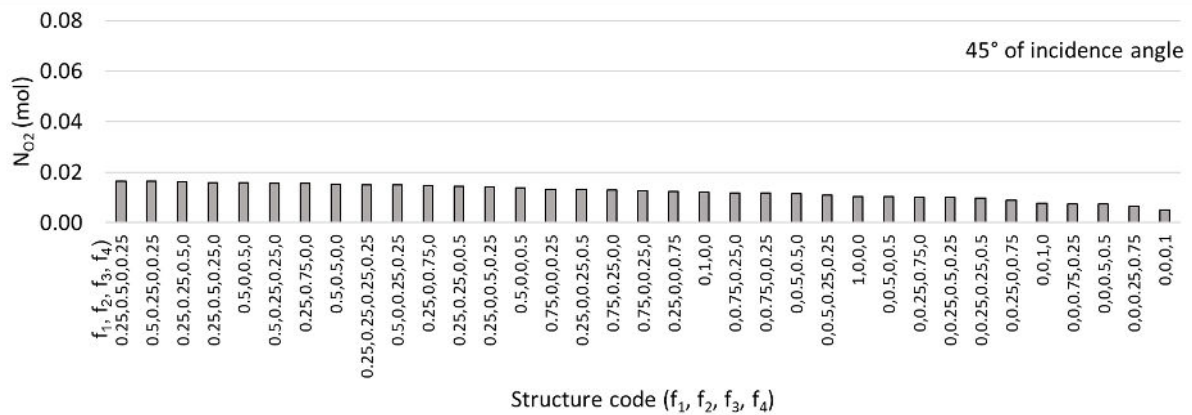


Figure 16: Ranking of the 35 arrangements for 45° incidence angle and flux of 1500 kW m⁻² in terms of number of mols released of O₂.

3.3. General trends – Irradiance

For the case of the general trend regarding different incidence irradiance intensities, the top-ranked structures (best structures) based on n_{O_2} (mol O₂/kg CeO₂) remain nearly identical. However, slight variations occur in the order of structures ranked from second to fourth place. Higher difference in the ranking of the structures for N_{O_2} is observed. The following figures shows the general trend for beam incidence angles of 5°, 15° and 30° for incidence flux of 1000 kW m⁻² and 500 kW m⁻² which details are to be addressed more in detail in the Section 3.4, where the ranking for the best structure for the different fluxes is presented.

3.4. Basic blocks ranking

The ranking of the arrangements of basic blocks for incident angles and irradiance according to the four figures of merit are presented below. Table 1, Table 2, Table 3 and Table 4 depict these figures at 1500 kW m⁻². These tables also including the corresponding information of the different figures of merit. Table 5 and Table 6 present the ranking of the arrangements at 1000 kW m⁻², while Table 7 and Table 8 show the results for a flux of 500 kW m⁻². The last four tables provide uniquely information on

expected oxygen released since this has been considered the most suitable figures of merit when evaluating performance under lower fluxes. Additionally, only incidence angles of 5°, 15° and 30° are analysed in these cases, as significantly lower performance is expected based on previous results for flux of 1500 kW m⁻². [Table 5](#), [Table 6](#), [Table 7](#), and [Table 8](#), the irradiance does not significantly change the top-ranked structures when n_{O_2} is considered, but a higher difference in the ranking of the structures for N_{O_2} is observed.

Table 1: Best arrangements in terms of released oxygen per unit mass of ceria for different incidence angles and an incident flux of 1500 kW m⁻².

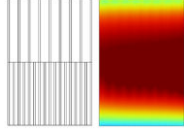
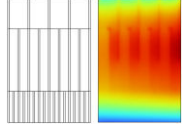
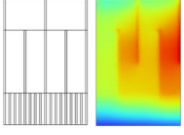
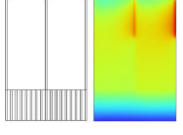
Incidence angle (°)	5°	15°	30°	45°
Arrangement (Total mass)	0.50,0.50,0.00,0.00 (75.47 g)	0.25,0.50,0.25,0.00 (59.63 g)	0.25,0.00,0.50,0.25 (44.88 g)	0.25,0.00,0.00,0.75 (38.65 g)
Temperature (°C)				
n_{O_2} (mol O ₂ /kg CeO ₂)	0.828	0.643	0.454	0.320
N_{O_2} (mol O ₂)	0.062	0.038	0.020	0.012
$\phi_{1600^\circ C}$ (Mass in g, %)	71.952 (95.3%)	51.114 (85.7%)	32.738 (73.0%)	22.437 (58.1%)
$\phi_{1000^\circ C}$ (Mass in g, %)	75.472 (100%)	59.633 (100%)	44.877 (100%)	38.266 (99.0%)

Table 2: Best arrangements in terms of released oxygen for different incidence angles and an incident flux of 1500 kW m⁻².

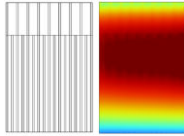
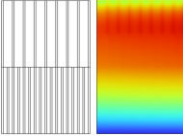
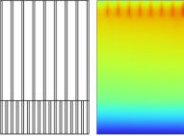
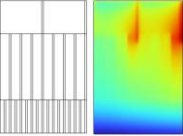
Incidence angle	5°	15°	30°	45°
Arrangement (Total mass)	0.75,0.25,0.00,0.00 (85.49 g)	0.50,0.50,0.00,0.00 (75.47 g)	0.25,0.75,0.00,0.00 (65.45 g)	0.25,0.50,0.00,0.25 (56.52 g)
Temperature (°C)				
n_{O_2} (mol O ₂ /kg CeO ₂)	0.783	0.548	0.375	0.290
N_{O_2} (mol O ₂)	0.067	0.041	0.025	0.0163
$\phi_{1600^\circ C}$ (Mass in g, %)	78.588 (91.9%)	57.464 (76.1%)	43.645 (66.7%)	31.089 (94.7%)
$\phi_{1000^\circ C}$ (Mass in g, %)	85.489 (100%)	74.519 (98.7%)	62.991 (96.2%)	53.541 (100%)

Table 3: Best arrangements in terms of fraction mass of zone at temperature higher than 1600 °C for different incidence angles and an incident flux of 1500 kW m⁻².

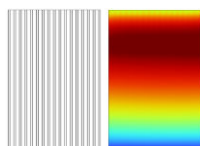
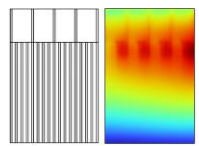
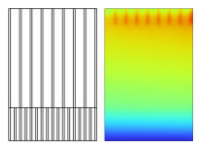
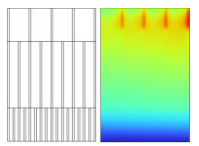
Incidence angle	5°	15°	30°	45°
Arrangement (Total mass)	1.00,0.00,0.00,0.00 (95.51 g)	0.75,0.00,0.25,0.00 (79.67 g)	0.25,0.75,0.00,0.00 (65.45 g)	0.25,0.50,0.25,0.00 (59.63 g)
Temperature (°C)				
n_{O_2} (mol O ₂ /kg CeO ₂)	0.694	0.513	0.375	0.267
N_{O_2} (mol O ₂)	0.066	0.041	0.025	0.016
$\phi_{1600\text{ °C}}$ (Mass in g, %)	80.779 (84.6%)	57.817 (72.6%)	43.645 (66.7%)	31.996 (53.7%)
$\phi_{1000\text{ °C}}$ (Mass in g, %)	95.506 (100%)	76.820 (96.4%)	62.991 (96.2%)	55.643 (93.3%)

Table 4: Best arrangements in terms of fraction mass of zone at temperature higher than 1000 °C for different incidence angles and an incident flux of 1500 kW m⁻².

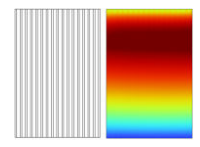
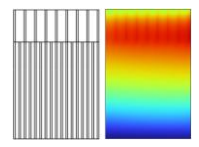
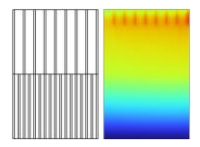
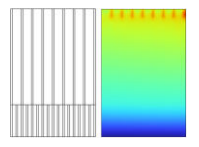
Incidence angle	5°	15°	30°	45°
Arrangement (Total mass)	1.00,0.00,0.00,0.00 (95.51 g)	0.75,0.25,0.00,0.00 (85.49 g)	0.50,0.50,0.00,0.00 (75.47 g)	0.25,0.75,0.00,0.00 (65.45 g)
Temperature (°C)				
n_{O_2} (mol O ₂ /kg CeO ₂)	0.694	0.454	0.324	0.239
N_{O_2} (mol O ₂)	0.066	0.039	0.024	0.016
$\phi_{1600\text{ °C}}$ (Mass in g, %)	80.779 (84.6%)	55.370 (64.8%)	41.354 (54.8%)	31.246 (47.7%)
$\phi_{1000\text{ °C}}$ (Mass in g, %)	95.506 (100%)	77.841 (91.1%)	66.924 (88.7%)	59.809 (91.4%)

Table 5: Best arrangements in terms of released oxygen per unit mass of ceria for different incidence angles and an incident flux of 1000 kW m⁻².

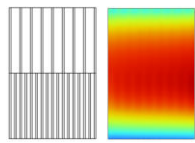
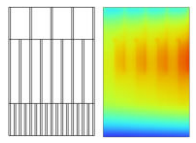
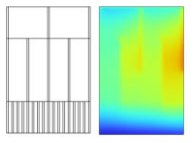
Incidence angle (°)	5°	15°	30°
Arrangement (Total mass)	0.50,0.50,0.00,0.00 (75.47 g)	0.25,0.50,0.25,0.00 (59.63 g)	0.25,0.00,0.50,0.25 (44.88 g)
Temperature (°C)			
n_{O_2} (mol O ₂ /kg CeO ₂)	0.699	0.451	0.263
N_{O_2} (mol O ₂)	0.053	0.027	0.012

Table 6: Best arrangements in terms of released oxygen per unit mass of ceria for different incidence angles and an incident flux of 500 kW m⁻².

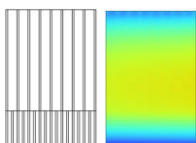
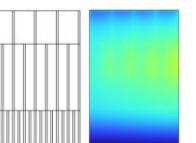
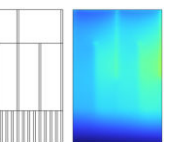
Incidence angle (°)	5°	15°	30°
Arrangement (Total mass)	0.25,0.75,0,0 (65.45 g)	0.25,0.5,0.25,0 (59.63 g)	0.25,0,0.5,0.25 (44.88 g)
Temperature (°C)			
n_{O_2} (mol O ₂ /kg CeO ₂)	0.338	0.119	0.053
N_{O_2} (mol O ₂)	0.022	0.007	0.002

Table 7: Best arrangements in terms of released oxygen for different incidence angles and an incident flux of 1000 kW m⁻².

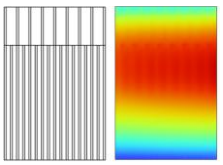
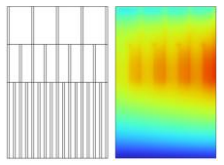
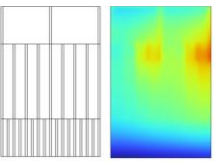
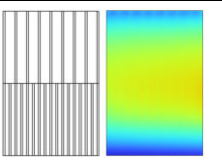
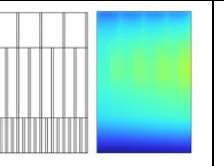
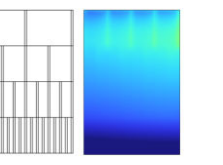
Incidence angle (°)	5°	15°	30°
Arrangement (Total mass)	0.75,0.25,0.00,0.00 (85.49 g)	0.50,0.25,0.25,0.00 (69.65 g)	0.25,0.50,0.00,0.25 (56.52 g)
Temperature (°C)			
n_{O_2} (mol O ₂ /kg CeO ₂)	0.619	0.400	0.231
N_{O_2} (mol O ₂)	0.053	0.028	0.013

Table 8: Best arrangements in terms of released oxygen for different incidence angles and an incident flux of 500 kW m⁻².

Incidence angle (°)	5°	15°	30°
Arrangement (Total mass)	0.50,0.50,0.00,0.00 (75.47 g)	0.25,0.5,0.25,0 (59.63 g)	0.25,0.25,0.25,0.25 (50.70 g)
Temperature (°C)			
n_{O_2} (mol O ₂ /kg CeO ₂)	0.330	0.119	0.050
N_{O_2} (mol O ₂)	0.025	0.007	0.003

The results of the ranked structures are consistent with the findings reported by Sas Brunser and Steinfeld (2023). The results obtained in our study will be subject of second validation in the experimental tasks of the project. Additionally, different optical errors at the released plane (angular perturbation of the rays) of 15.70 mrad, 30.36 mrad and 60.18 mrad for the different incidence angles were also analysed, but the ranking of the structures remained unchanged.

4. Conclusions and Outlook

This work presents a detailed time-dependent numerical model for heat and mass transfer in novel porous structures composed of ceria. The model focuses on the reduction step that is performed under vacuum and concentrated sunlight. Concentrated solar radiation heat transfer is solved by ray tracing. Radiation heat transfer (due to the infrared contribution) and conduction heat transfer in the solid are solved using Computational Fluid Dynamics (CFD). Mass transfer related to the oxygen released in the reduction of the material is computed using the resulting temperature field and temperature dependent stoichiometric correlations.

The porous structure is based on a stack of square channel monoliths with a decreasing channel size to promote radiation absorption and an homogeneous temperature distribution. Simulations reveal that at low incidence angles ($\sim 5^\circ$), the optimal basic block consists of two layers of half height each. The lower layer is composed of 16×16 (finer) channels and the top layer of 8×8 channels. When incidence angles approach but still below 30° , a third layer of 4×4 channels becomes advantageous. At higher angles (higher than 30°), 2×2 (larger) channels become relevant, indicating that larger channels are needed to allow deeper radiation penetration and achieve a truly volumetric heating effect. In these cases, the 4×4 layer becomes unnecessary.

Regarding the influence of the incident solar flux, the best arrangements in terms of moles of O_2 released per kilogram of CeO_2 remains consistent for lower fluxes. More significant changes are observed when the figure of merit is the total moles of O_2 released. Overall, the findings are valuable for designing a first generation, lab scale solar reactor based on a basic block concept in which the different structures for varying incidence angles and concentrated solar fluxes can be combined to simulate full reactor behaviour by incorporating a cavity effect factor.

5. References

- [1] P. Furler and A. Steinfeld, "Heat transfer and fluid flow analysis of a 4 kW solar thermochemical reactor for ceria redox cycling", *Chemical Engineering Science*, vol.137, 2015, <https://doi.org/10.1016/j.ces.2015.05.056>
- [2] S. Sas Brunser and A. Steinfeld, "Design and Optimization of Hierarchically Ordered Porous Structures for Solar Thermochemical Fuel Production Using a Voxel-Based Monte Carlo Ray-Tracing Algorithm", *ACS Engineering Au*, vol.3 (5), 2023, <https://doi.org/10.1021/acsengineeringau.3c00013>
- [3] S. Zoller, E. Koepf, D. Nizamian, M. Stephan, A. Patané, P. Haueter, M. Romero, J. González-Aguilar, D. Liefstink, E. de Wit, S. Brendelberger, A. Sizmann, and A. Steinfeld, "A solar tower fuel plant for the thermochemical production of kerosene from H₂O and CO₂", *Joule* vol.6 (7), 2022, <https://doi.org/10.1016/j.joule.2022.06.012>